Computational Fluid Dynamics Simulation of Deep-Water Wave Instabilities Involving Wave Breaking

Li, Yuzhu; Fuhrman, David R.

Published in:
Journal of Offshore Mechanics and Arctic Engineering

Link to article, DOI:
10.1115/1.4052277

Publication date:
2022

Document Version
Peer reviewed version

Journal of Offshore Mechanics and Arctic Engineering. Received May 17, 2021;
Accepted manuscript posted August 20, 2021. doi:10.1115/1.4052277

CFD Simulation of Deep-Water Wave Instabilities Involving Wave Breaking

Yuzhu Li*
Section for Fluid Mechanics, Coastal and Maritime Engineering
Department of Mechanical Engineering
Technical University of Denmark
DK-2800 Kgs. Lyngby, Denmark
Email: yuzhuli@mek.dtu.dk

David R. Fuhrman
Section for Fluid Mechanics, Coastal and Maritime Engineering
Department of Mechanical Engineering
Technical University of Denmark
DK-2800 Kgs. Lyngby, Denmark
Email: drf@mek.dtu.dk

Instabilities of deep-water wave trains subject to initially small perturbations (which then grow exponentially) can lead to extreme waves in offshore regions. The present study focuses on the two-dimensional Benjamin–Feir (or modulational) instability and the three-dimensional crescent (or horseshoe) waves, also known as Class I and Class II instabilities, respectively. Numerical studies on Class I and Class II wave instabilities to date have been mostly limited to models founded on potential flow theory, thus they could only properly investigate the process from initial growth of the perturbations to the initial breaking point. The present study conducts numerical simulations to investigate the generation and development of wave instabilities involving the wave breaking process. A computational fluid dynamics (CFD) model solving Reynolds-averaged Navier-Stokes (RANS) equations coupled with a turbulence closure model in terms of the Reynolds stress model is applied. Wave form evolutions, Fourier amplitudes, and the turbulence beneath the broken waves are investigated.

1 Introduction

Extreme waves can sometimes be encountered in the offshore deep-water regions. They can have severe impacts on offshore structures (e.g. ships, offshore platforms) by causing wave over-topping, imparting extreme slamming loads, and affecting the stability of the structure. Therefore, it is of fundamental importance and practical interest to understand, and be able to model, the mechanisms potentially causing their occurrence in ocean and offshore conditions. One of the theoretical mechanisms leading to extreme waves is the instability of deep-water wave trains subject to initially small perturbations, which then grow exponentially. Under certain conditions, wave breaking will occur. Benjamin and Feir [1] first showed that weakly nonlinear deep-water waves can be unstable to two-dimensional (2D) modulational perturbations. McLean [2] classified the so-called Benjamin-Feir wave instability as Class I instability, which is generally strongest in the case of a plane wave train subject to 2D perturbations. Tulin and Waseda [3] conducted a massive study of seeded experiments of wave train evolutions, where the modulation naturally evolved from background noise in their experiments. They observed an overall decrease in the amplitude of the carrier wave, with an increase in the wave amplitude of the lower sideband (i.e. perturbation of frequency lower than the carrier wave frequency). Hwung et al. [4] further conducted a longer-time experiment to investigate a long time evolution of the Benjamin-Feir instability, and they confirmed the phenomenon of permanent frequency downshift after wave breaking. Madsen et al. [5] numerically reproduced the experiments of Tulin and Waseda [3] and investigated the Benjamin-Feir (or modulational) instability with a nonlinear potential flow theory based Boussinesq model. They reproduced the phenomenon of recurrence of the sidebands growth (with energy exchange between carrier wave and sidebands) in the case without wave breaking. For steeper waves involving breaking, their fine-grid simulation broke down. Therefore, they had to use a relatively coarse grid resolution to trigger a certain amount of numerical dissipation (instead of turbulent dissipation) in order for the simulation to survive the breaking process. The numerical study of Madsen et al. [5] indicates the necessity of proper turbulence modelling for studying wave instability involving the wave breaking process. To investigate the modulation process that goes beyond wave breaking, Iafrati et al. [6, 7] and Alberello and Iafrati [8] modelled the Benjamin-Feir instability with wave breaking using a combined method. They adopted a fully nonlinear potential flow model to simulate the modulational instability up to the breaking point. Then a 2D Navier-Stokes solver for two-phase flows (i.e. air and water) were used to simulate the further evolution of the modulated

*Address all correspondence to this author. Email: yuzhuli@mek.dtu.dk

waves. In contrast to the works of [6, 7, 8], De Vita et al. [9] conducted a 2D simulation for the modulational instability using the two-phase Navier-stokes solver from the very beginning of the wave evolution. In this way, the transition from non-breaking potential flow to breaking was solved in a smoother manner. It is emphasized, however, that such 2D Navier-Stokes simulations (at least in the absence of a turbulence model) cannot fully account for effects of turbulence post-breaking, since turbulence is inherently three dimensional. In order to explore the regime of large wave lengths to reduce the role of surface tension of breaking [10], De Vita et al. [9] adopted a wave length of 0.6 m (much larger comparing to 0.24 m in the numerical study of Deike et al. [11], although is still shorter than the wave length 1.2 m in the experiment of Tulin and Waseda [3]). In order to further reduce the computational time, De Vita et al. [9] considered a relatively high initial steepness to reach the breaking point earlier than in the Tulin and Waseda's experiments [3]. Due to the high computational cost for conducting 2D Navier-Stokes simulations without using a turbulence model, their simulations were ended shortly after wave breaking while frequency downshift still persists.

Another type of wave instability of interest leads to predominantly three-dimensional (3D) crescent waves, also known as Class II instability according to McLean [2]. Numerical simulations of crescent waves using a boundary-element model were performed by Xue et al. [12], in which their investigation was limited to relatively small domains and short time scales. Fuhrman et al. [13] studied crescent waves with a high-order Boussinesq model at somewhat larger spatial and temporal scales, providing new insight into the physical processes involved. Later, Fructus et al. [14], Xu and Guyenne [15] and Klahn et al. [16] have also simulated such phenomenon based on potential flow equations. To the authors' knowledge, seemingly all of the numerical studies on Class II wave instabilities to date have been limited to models founded on potential flow theory, thus they could only properly investigate the process from initial growth of the perturbations to the initial breaking point [5, 12, 13, 14, 15, 16].

The present study will conduct computational fluid dynamics (CFD) simulations to investigate the phenomena of both Class I and Class II deep-water wave instabilities involving wave breaking in a detailed manner. One of the experiments of Tulin and Waseda [3] for Benjamin-Feir (Class I) wave instability of a weakly-nonlinear plane wave subjected to 2D disturbances will be numerically reproduced. The simulation of 3D crescent waves will likewise generate the common phase-locked (L2) patterns experimentally observed by e.g. Su [17]. The open-source CFD wave generation toolbox `waves2foam` [18] developed in the `OpenFOAM v1812` framework will be used to conduct simulations. The free-surface (i.e. the interface between air and water) is captured using the volume of fluid (VOF) method.

As the wave instabilities will involve turbulence after initial breaking, a model solving Reynolds-averaged Navier-Stokes (RANS) equations coupled with the anisotropic Reynolds stress turbulence model (RSM) i.e. the Wilcox (2006) stress-ω model [19] will be applied, where ω is the specific turbulence dissipation rate. The stress-ω turbulence model is used because it has been proved to be neutrally stable in the potential flow region beneath surface waves [20]. Previous works using two-equation models (both standard k-ω and k-ε types, where k is the turbulence kinetic energy, and ε is the turbulence dissipation rate) [21, 22, 23, 24] have shown a persistent problem of over-production of turbulence in the potential flow region beneath non-breaking surface waves, which causes the progressive waves to decay during long-time simulation even before reaching the wave breaking point. Larsen and Fuhrman [25] have analyzed almost all of the two-equation models and found that they are "unconditionally" unstable in the potential flow region beneath surface waves. They have then formally stabilized the two-equation models by reformulating the eddy viscosity. Fuhrman and Li [26] analyzed a more complicated but also commonly used two-equation model - the realizable k-ε model [27], and they proved that it is "conditionally" unstable in such regions. They have likewise stabilized the realizable k-ε model. In contrast to two-equation RANS models, the RSM models break free from the Boussinesq approximation, thus they were proved to be neutrally stable for simulating non-breaking progressive wave trains [20] without having the problem of over-production of turbulence in the potential flow region beneath surface waves. The RSM model has also achieved excellent accuracy in the prediction of coastal breaking waves on a sloped beach, especially the undertow velocity, as presented in the work of [28, 20].

With using the present CFD model, the physical process of wave instabilities involving wave breaking will be simulated. Wave forms evolutions, Fourier amplitudes, and the turbulence beneath the broken waves will be investigated. Since the present CFD model is able to accurately simulate the entire breaking process, the during- and post-breaking evolution of deep-water wave instabilities can be studied in a proper manner, thus extending previous investigations based on nonlinear potential flow theories.

2 Theoretical Background and Mathematical Equations

2.1 The Two-Dimensional Benjamin-Feir Instability

As observed in the work of [1, 3, 2], deep-water waves may develop instabilities under sideband perturbations whenever the resonance conditions are satisfied, which leads to disintegration of the original wave form. This will produce resonance where the sideband waves can grow exponentially. According to [2], the strongest Class I instabilities are actually 2D which was first showed by Benjamin and Feir [1] therefore commonly known as the Benjamin-Feir instability. It can be described as quartet resonant interactions between a carrier wave and two small disturbances satisfying the following condition:

$$\boldsymbol{k}_1 + \boldsymbol{k}_2 = 2\boldsymbol{k}_0, \tag{1}$$

Journal of Offshore Mechanics and Arctic Engineering. Received May 17, 2021;
Accepted manuscript posted August 20, 2021. doi:10.1115/1.4052277

$$\omega_1 + \omega_2 = 2\omega_0 \tag{2}$$

where $\boldsymbol{k}_0 = \langle k_0, 0\rangle$ and ω_0 are the carrier wave number and frequency; $\boldsymbol{k}_1 = \langle k_1, 0\rangle$, $\boldsymbol{k}_2 = \langle k_2, 0\rangle$, and $\omega_{1,2}$ are the wave numbers and frequencies of two small perturbations, respectively. Note that in the present paper, the k and ω without subscripts denote the kinetic energy and specific dissipation rate of turbulence, as defined in Section 1. The propagation of each wave component is along the same direction.

It was found by McLean [2] that the Benjamin-Feir type of instability is dominant for relatively small amplitude waves where the carrier wave can be described by linear wave theory. A Stokes wave train travelling in the x direction consisting of a carrier wave and two small-amplitude sideband waves can be expressed as [5]:

$$\eta = a_0 \cos(\omega_0 t - k_0 x) + \xi a_0 \cos\Theta_1 + \xi a_0 \cos\Theta_2 \tag{3}$$

$$\Theta_1 = \omega_0(1+\delta)t - k_1 x + \Psi_1 \tag{4}$$

$$\Theta_2 = \omega_0(1-\delta)t - k_2 x + \Psi_2 \tag{5}$$

$$k_1 = k_0(1+\delta)^2,\ k_2 = k_0(1-\delta)^2 \tag{6}$$

where δ is small. In the equations above, η is the wave elevation, a_0 is the wave amplitude of the carrier wave, ξ is the normalized amplitude of the perturbation relative to the carrier wave amplitude. For linear deep-water waves,

$$k_0 = \frac{\omega_0^2}{g} \tag{7}$$

where g is the gravitational acceleration.

2.2 The Three-Dimensional L2 Crescent Waves

The crescent (also called 'horseshoe' due to the wave shape) waves are a result of fully nonlinear 3D wave interactions. In the present study, we consider the most unstable (also most commonly seen) phase-locked L2 crescent patterns (i.e. the wave pattern is repeated every other carrier wave length [17,29]). Quintet resonant condition is the dominant physical process for the L2 crescent patterns, which satisfies:

$$\boldsymbol{k}_1 + \boldsymbol{k}_2 = 3\boldsymbol{k}_0 \tag{8}$$

$$\omega_1 + \omega_2 = 3\omega_0 \tag{9}$$

where $\boldsymbol{k}_0 = \langle k_0, 0\rangle$ is the wave number of the central harmonic or the carrier wave. In the general L2 case, $\boldsymbol{k}_1 = \langle k_x, k_y\rangle$ and $\boldsymbol{k}_2 = \langle k_x, -k_y\rangle$ are two symmetric oblique satellites.

According to McLean [2], the instability is predominantly 3D (Class II) for fully nonlinear steep waves. Following the numerical study in Fuhrman et al. [13], the crescent waves are generated by superimposing the 3D perturbations to a stream-function solution [30] for a plane wave travelling in the x direction. The perturbation function is expressed as follows:

$$\eta' = \frac{\epsilon H_0}{2} \sin(k_x x)\cos(k_y y) \tag{10}$$

where ϵ is the relative perturbation amplitude, H_0 is the carrier wave height. According to McLean [2], the most unstable disturbance for this type of instability occurs at $k_x = 1.5k_0$ and $k_y \neq 0$.

2.3 Turbulence Closure Model

To simulate wave instability involving the wave breaking process, the present CFD model is built by solving the incompressible unsteady Reynolds-averaged Navier-Stokes (URANS) equations together with an anisotropic Reynolds stress turbulence closure model i.e. the Wilcox (2006) stress-ω model [19]. The Wilcox (2006) stress-ω model has been proved to be neutrally stable in regions of nearly potential flow with finite strain [20], unlike standard two-equation models that were proved to be unconditionally [25] or conditionally [26] unstable in such regions. Therefore, the Wilcox (2006) stress-ω model is applied for simulating surface waves in the present work. The equations of the Wilcox (2006) stress-ω model [19] consisting of six equations for Reynolds stresses τ_{ij} and one equation for ω are as follows:

$$\begin{aligned}\frac{\partial \bar{\rho}\tau_{ij}}{\partial t} + \bar{u}_k \frac{\partial \bar{\rho}\tau_{ij}}{\partial x_k} &= -\bar{\rho}P_{ij} + \frac{2}{3}\bar{\rho}\beta^*\omega k\delta_{ij} - \bar{\rho}\Pi_{ij} \\ &+ \frac{\partial}{\partial x_k}\left[\bar{\rho}(\nu + \sigma^*\frac{k}{\omega})\frac{\partial \tau_{ij}}{\partial x_k}\right] + \bar{\rho}\alpha_b^*\frac{k}{\omega}N_{ij}\end{aligned} \tag{11}$$

$$\begin{aligned}\frac{\partial \bar{\rho}\omega}{\partial t} + \bar{u}_j \frac{\partial \bar{\rho}\omega}{\partial x_j} &= \bar{\rho}\alpha\frac{\omega}{k}\tau_{ij}\frac{\partial \bar{u}_i}{\partial x_j} - \bar{\rho}\beta\omega^2 + \sigma_d\frac{\bar{\rho}}{\omega}\frac{\partial k}{\partial x_j}\frac{\partial \omega}{\partial x_j} \\ &+ \frac{\partial}{\partial x_k}\left[\bar{\rho}(\nu + \sigma\frac{k}{\omega})\frac{\partial \omega}{\partial x_k}\right]\end{aligned} \tag{12}$$

The pressure-strain correlation is:

$$\begin{aligned}\Pi_{ij} = \beta^* C_1 \omega\left(\tau_{ij} + \frac{2}{3}k\delta_{ij}\right) - \hat{\alpha}(P_{ij} - \frac{2}{3}P\delta_{ij}) \\ -\hat{\beta}(D_{ij} - \frac{2}{3}P\delta_{ij}) - \hat{\gamma}k(S_{ij} - \frac{1}{3}S_{kk}\delta_{ij})\end{aligned} \tag{13}$$

where

$$P_{ij} = \tau_{im}\frac{\partial \bar{u}_j}{\partial x_m} + \tau_{jm}\frac{\partial \bar{u}_i}{\partial x_m} \tag{14}$$

$$D_{ij} = \tau_{im}\frac{\partial \bar{u}_m}{\partial x_j} + \tau_{jm}\frac{\partial \bar{u}_m}{\partial x_i} \tag{15}$$

$$S_{ij} = \frac{1}{2}\left(\frac{\partial \bar{u}_i}{\partial x_j} + \frac{\partial \bar{u}_j}{\partial x_i}\right) \tag{16}$$

$$P = \frac{1}{2}P_{kk} \tag{17}$$

$$k = -\frac{1}{2}\tau_{kk} \tag{18}$$

In the present work, the Reynolds stress tensor is denoted by $\bar{\rho}\tau_{ij}$, where τ_{ij} is the specific Reynolds stress tensor defined as

$$\tau_{ij} = -\overline{u_i' u_j'} \tag{19}$$

where the overbar denotes Reynolds (ensemble) averaging. Note that τ_{ij} also appears directly in the RANS governing equations, and is therefore through this quantity that the turbulence model affects the hydrodynamic model. The last term in Eqn. (11) is the buoyancy production term as derived in [20] which is proportional to the Brunt-Väisälä frequency tensor:

$$N_{ij} = \frac{1}{\rho_0}\left(g_i\frac{\partial \bar{\rho}}{\partial x_j} + g_j\frac{\partial \bar{\rho}}{\partial x_i}\right) \tag{20}$$

In the equations above, x_j are the Cartesian coordinates, $\bar{u}_j$ are the mean components of the velocity, u_j' are the fluctuating velocity, g_j are the gravitational acceleration, ν is the kinematic viscosity, $\bar{\rho}$ is the density, ρ_0 is the constant reference density of the fluid, t is time, and S_{ij} is the mean strain rate tensor. The closure coefficients are [19, 20]:

$$\begin{aligned} C_1 = 1.8, \quad C_2 = 10/19, \quad \hat{\alpha} = (8+C_2)/11, \\ \hat{\beta} = (8C_2-2)/11, \quad \hat{\gamma} = (60C_2-4)/55, \quad \alpha = 0.52, \\ \beta^* = 0.09, \quad \beta_0 = 0.0708, \quad \beta = \beta_0 f_\beta, \\ \sigma = 0.5, \quad \sigma^* = 0.6, \quad \sigma_{d0} = 0.125, \\ \alpha_b^* = 1.36 \end{aligned} \tag{21}$$

	Wave length λ (m)	Wave period T (s)	Wave height H (m)
Carrier wave	1.2	0.87	0.0508
Upper sideband	1.0	0.8	0.00254
Lower sideband	1.5	0.98	0.00254

Table 1: Wave parameters input for the simulation of Benjamin-Feir instability based on the Tulin and Waseda's experiment [3].

$$\sigma_d = \begin{cases} 0, & \dfrac{\partial k}{\partial x_j}\dfrac{\partial \omega}{\partial x_j} \le 0 \\ \sigma_{d0}, & \dfrac{\partial k}{\partial x_j}\dfrac{\partial \omega}{\partial x_j} \ge 0 \end{cases} \tag{22}$$

$$\begin{aligned} f_\beta &= \frac{1+85\chi_\omega}{1+100\chi_\omega}, \\ \chi_\omega &= \left|\frac{\Omega_{ij}\Omega_{jk}\hat{S}_{ki}}{(\beta^*\omega)^3}\right|, \\ \hat{S}_{ki} &= S_{ki} - \frac{1}{2}\frac{\partial \bar{u}_m}{\partial x_m}\delta_{ki} \end{aligned} \tag{23}$$

3 CFD Simulation of the Benjamin-Feir Instability

3.1 Numerical Setup

Tulin and Waseda [3] conducted a series of seeded experiments to investigate the Benjamin-Feir instability of deep water wave trains. Without wave breaking, they have noticed a recurrence phenomenon as modelled numerically in the work of Madsen et al. [5]. Conversely, for experiments with local wave breaking, they observed a permanent downshift of the peak frequency. Namely, after breaking the carrier wave and upper sideband amplitudes decreased, whereas the amplitude of the lower sideband permanently increased. In the present study, we will simulate one of the tests from Tulin and Waseda [3] involving wave breaking. The carrier wave has wave length $\lambda_0 = 1.2$ m and wave steepness $k_0 a_0 = 0.133$, where $a_0 = H_0/2 = 0.0254$ m. The perturbations are designed on the basis of $\delta = 0.785 k_0 a_0$ and with relative amplitude $\xi = 0.03$ following the numerical study in Madsen et al. [5]. The length of the wave tank is set as 6 m i.e. $5\lambda_0$, and the depth of the numerical tank is set as $h = \lambda_0$ (hence $k_0 h = 2\pi$) to be well beyond the practical deep-water limit. The wave properties used as input to `OpenFOAM` for the carrier wave and sideband waves are provided in Table 1. The initial waves are specified based on the stream-function solutions [30].

The numerical wave tank as shown in Fig. 1 is built in a uniform Cartesian coordinate system with x positive corresponding to the direction of carrier wave propagation, y

Journal of Offshore Mechanics and Arctic Engineering. Received May 17, 2021;
Accepted manuscript posted August 20, 2021. doi:10.1115/1.4052277

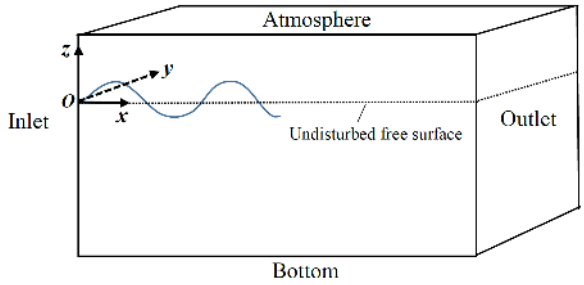

Fig. 1: The layout of the three-dimensional numerical wave tank with carrier wave propagating along the x positive direction.

positive toward the side of the tank, and z positive upwards with $z = 0$ the undisturbed free surface. The open-source CFD wave generation toolbox `waves2foam` [18] developed in the `OpenFOAM v1812` framework is used to simulate the wave initiation and propagation process. The boundary conditions are specified as follows:

- At the inlet and outlet, cyclic (periodic) boundary conditions are applied.
- At the atmosphere, the uniform pressure is applied with its value equal to the atmosphere pressure and the velocity of zero-gradient.
- At the bottom of the wave tank, slip boundary condition is specified as deep-water waves are considered.

Based on a preliminary grid convergence study, the numerical grid resolution for the 2D simulation of Benjamin-Feir instability is set with 180 cells per wave length and 25 grids per wave height. The total number of grid cells is 157,500. It is worthwhile to mention that the number of cells used in [9] is 2^{11} per wave length. Our present study using a RANS approach accounts for turbulence effects more efficiently.

Since the present study consists of a free surface, the Courant number is set as 0.01 to achieve stable and accurate wave elevation results based on our preliminary convergence study. This is generally in accordance with small Courant numbers recommended by Larsen et al. [31]. The initial turbulence quantities are set as low as $k/(\omega\nu) = 0.1$, where $\nu = 10^{-6}$ m^2/s is the kinematic viscosity of water. The simulated Benjamin-Feir instability case (up to 150 wave periods) required approximately 6 days to run in parallel on 16 processors on the supercomputing cluster at the Technical University of Denmark (DTU).

3.2 Results and Analysis

The present numerical reproduction for the test case of Tulin and Waseda [3] involves a brief event of wave breaking at around the first modulational peak. First, to validate the present CFD model, the spatial evolution of the wave train is plotted and is compared with the experimental data of Tulin and Wadeda [3]. The exponential growth rate of the sidebands is also verified against the analytical prediction of Benjamin and Feir [1], as shown in Fig. 2. Since the experimental results of Tulin and Waseda [3] were presented in the spatial domain, we transform our results from time domain to the spatial domain following Madsen et al. [5] using the following relation:

$$\frac{x}{\lambda} = \frac{c_g t}{cT} \approx \frac{1}{2}\frac{t}{T} \tag{24}$$

where c_g is the group velocity and c is the celerity.

It is observed in Fig. 2 that the initial growth rate of the sidebands agrees well with the theoretical prediction. The theoretical amplitude for the growing sidebands during the initial stage is expressed as [1]:

$$\frac{a}{a_0} = \xi e^{\delta (2k_0^2 a_0^2 - \delta^2)^{\frac{1}{2}} k_0 x} \tag{25}$$

The initial evolutions of the carrier wave and the sidebands also match very well with the experimental data of Tulin and Waseda [3]. During the resonant interaction, it is seen in Fig. 2 that the lower sideband grows to a level at around $0.8a_0$, which is in good agreement with the experiment. Wave breaking was observed around $k_w x/(2\pi) = 40$, where k_w is the wave number. After the occurrence of wave breaking, the amplitude of the lower sideband slightly decreases but remains to be higher than that of the carrier wave. Moreover, the carrier wave shows the behaviour described by Tulin and Waseda [3] that after wave breaking, it decreases to a local minimum and then rises but not back to its original strength. This phenomenon is also observed in the experiments of e.g. Melville [32]. Figure 3 further presents the present simulation results over a longer time evolution ($t/T \approx 150$) than were measured in the experiment. It is seen that the amplitude of the lower sideband remains the highest, while the carrier wave and upper sideband amplitudes fluctuate, but remain much lower than the lower sideband. Therefore, it can be confirmed that a permanent frequency downshift has occurred after waves breaking around the peak of the modulation. The present findings using a CFD model are consistent with the long-time measurement and analytical prediction of wave evolution in Hwung et al. [4]. These results are the first to simulate this long term evolution using a model which properly simulate the breaking process.

Figure 4 presents the wave profile over the simulated domain and the corresponding Fourier amplitudes at different time instants. It is seen that near the initial time (Fig. 4a), the sideband amplitudes are insignificant compared to the carrier wave. The sidebands then grow gradually but exponentially, extracting energy from the carrier wave (Fig. 4b). The interaction between carrier wave and sidebands further activates the growth of other wave components spreading over more wave numbers. Figure 4(c) shows a time when the lower sideband amplitude exceeds that of the carrier wave. A steep wave emerges in the simulated domain with its wave amplitude

Journal of Offshore Mechanics and Arctic Engineering. Received May 17, 2021;
Accepted manuscript posted August 20, 2021. doi:10.1115/1.4052277

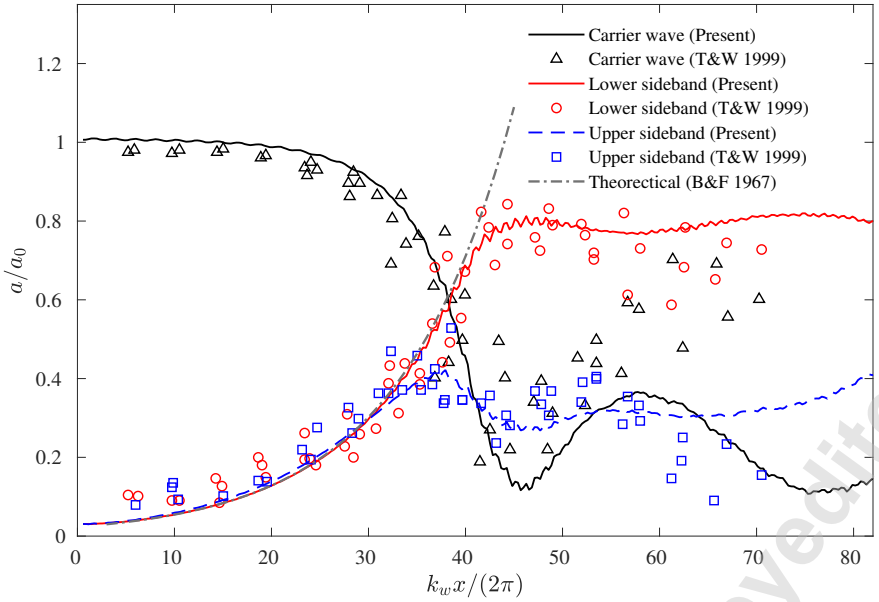

Fig. 2: Spatial evolution of the carrier wave and sideband wave amplitudes. In the legend, T&W 1999 denotes the experimental data of Tulin and Waseda [3], and B&F 1967 denotes the theoretical prediction of the sideband growth rate from Benjamin and Feir [1].

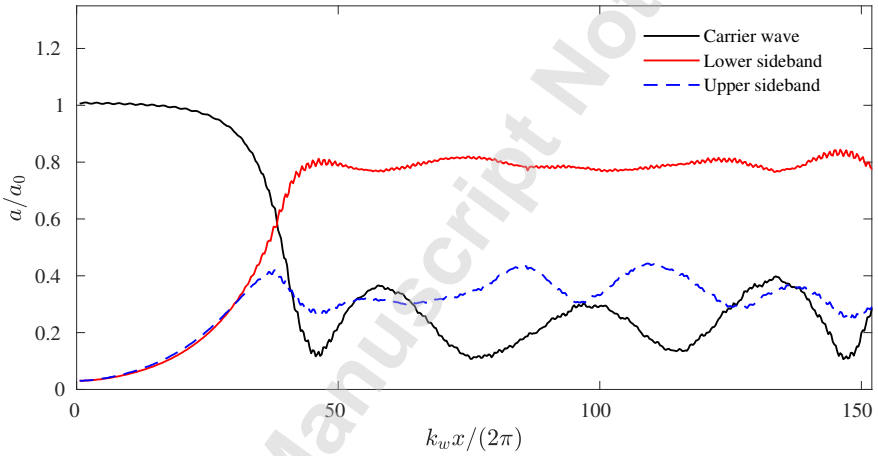

Fig. 3: Long-time simulation of spatial evolution of the carrier wave and sideband wave amplitudes.

2.5 times the initial wave amplitude. Wave breaking occurs around this time instant and will be shown later. Figure 4(d-e) present time instants after wave breaking, demonstrating a permanent frequency downshift, i.e. the amplitude of wave component $k/k_0 = 0.785$ remains higher than that of $k/k_0 = 1$ and other wave components.

Figure 5 further shows snapshots of the wave profile and turbulence level beneath the waves in the simulated domain. It is seen that during the initial development (Fig. 5a), the waves are in a Stokes pattern with no turbulence production beneath the surface. In this region, the potential flow theory is valid. The spilling breaking process occurs when the wave becomes very steep, as shown in Fig. 5(b). The wave breaking process is accompanied with turbulent kinetic energy production beneath the surface waves. Once the onset of wave breaking occurs, a potential flow theory based model will break down. The spilling breaking event here is rather brief and mild without much overturning of the crest. Therefore, the turbulence production beneath the broken wave is also relatively mild. The crescent shape in Fig. 5(b) for the first breaking event is very similar to that presented in [9] (their Fig. 4). Figure 5(c) shows a post-breaking time instant where the carrier wave has decayed and the lower sideband amplitude has increased, and breaking has ceased. At this stage, the turbulence kinetic energy is continuously diffused downward from near-surface regions. Figure 5(d) shows a time step around 40 periods after wave breaking, where the turbulent kinetic energy has been dissipated to an almost zero level.

Overall, the CFD simulation of the Benjamin-Feir in-

Journal of Offshore Mechanics and Arctic Engineering. Received May 17, 2021;
Accepted manuscript posted August 20, 2021. doi:10.1115/1.4052277

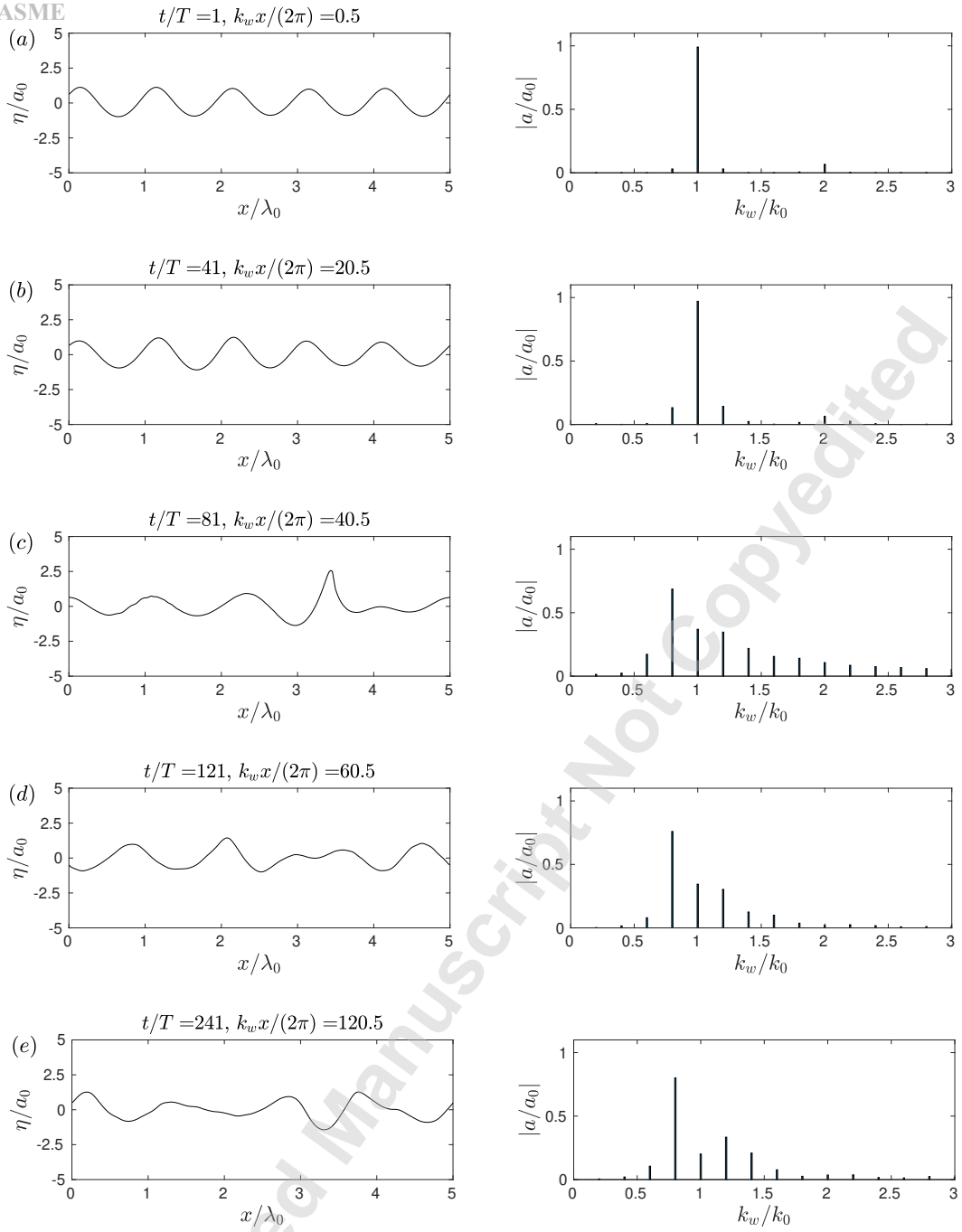

Fig. 4: Wave profiles over the simulated domain and the corresponding Fourier amplitudes at different time instants for the Benjamin-Feir instability.

stability involving wave breaking demonstrates reasonably accurate results which are in agreement with the previous experiment of Tulin and Waseda [3]. The present CFD prediction of the exponential growth rate of the sidebands is also verified against the analytical prediction. Compared to the previous numerical models based on the potential flow theory, the present CFD model with the Wilcox (2006) stress-ω turbulence closure model can well capture the wave breaking phenomenon arising from the instability and is able to predict the long-time wave evolution (including the frequency downshift phenomenon) after breaking.

4 CFD Simulation of L2 Crescent Waves

4.1 Numerical Setup

We will now focus on the CFD simulation of Class II wave instability, leading to fantastic three-dimensional crescent surface waves. The present crescent wave simulation starts with a fully nonlinear deep-water wave of $k_0 a_0 = 0.33$ and wave number $k_0 = 1.0\,\mathrm{m}^{-1}$. The wave steepness of H_0/λ_0

Journal of Offshore Mechanics and Arctic Engineering. Received May 17, 2021;
Accepted manuscript posted August 20, 2021. doi:10.1115/1.4052277

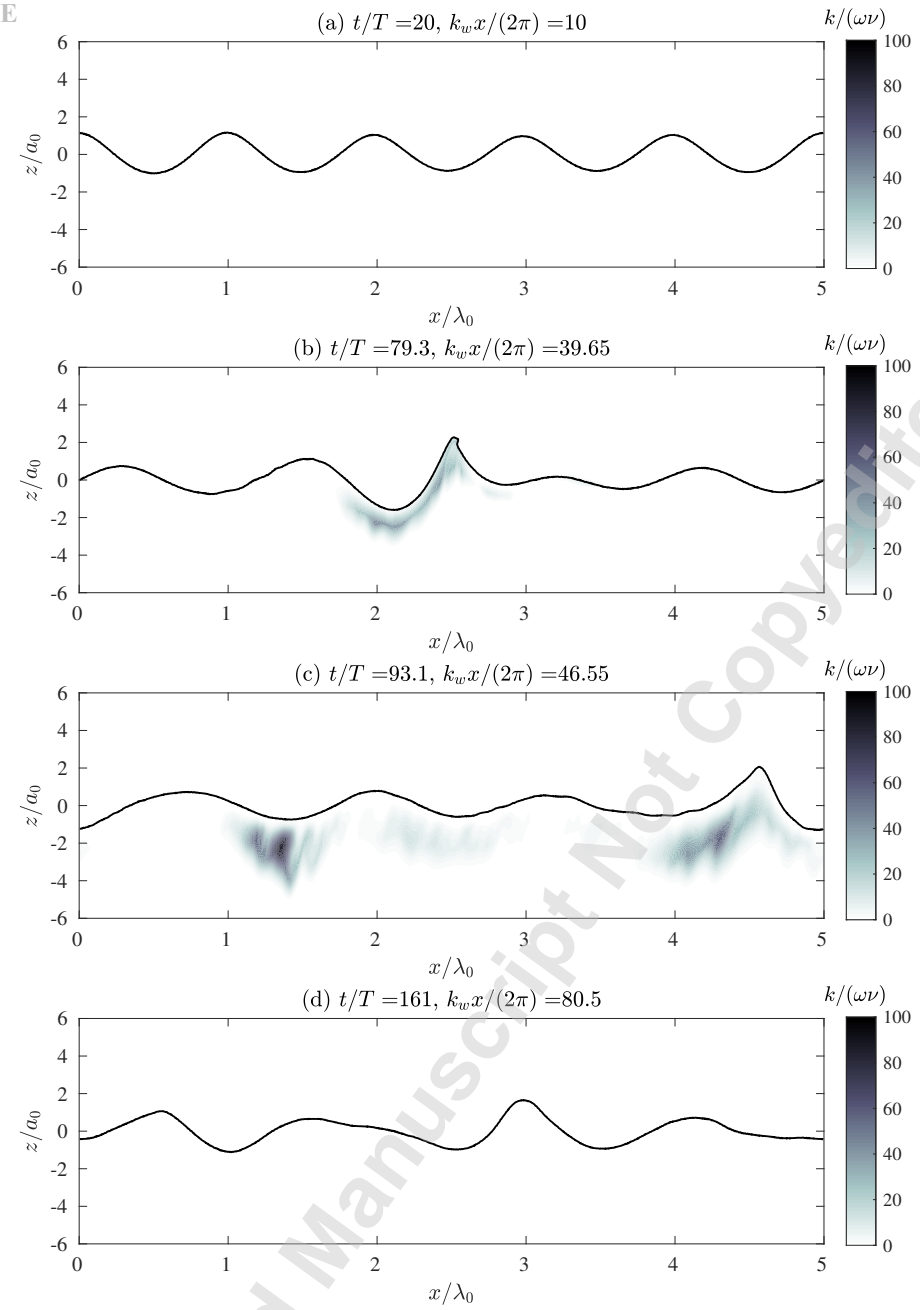

Fig. 5: Turbulence levels indicated by $k/(\omega\nu)$ beneath the surface waves during the nonlinear evolution of the Benjamin-Feir instability.

is 0.105, where $\lambda_0 = 2\pi$ m is the carrier wave length. The satellite (perturbation) wave numbers are set as $k_x = 1.5k_0$ and $k_y = 1.23$ m^{-1}. According to McLean [2], this corresponds to the most unstable Class II mode for this wave steepness. The perturbation amplitude is set to be small with $\epsilon = 0.05$ in order to clearly simulate the generation and development process of the crescent waves. For the 3D crescent wave simulation, the layout of the numerical wave tank is the same as that in Fig. 1. The water depth is set as $h = \lambda_0$ to be in the deep-water condition. The domain length for the wave tank is set to $2\lambda_0$, and the domain width is set as half of crescent width i.e. $L_y = \pi/k_y$ as the crescent pattern is symmetric about its centreline. The waves are likewise initiated with stream-function solutions [30]. Based on earlier grid convergence study, the cell number per wave height is set as 30 and per wave length is set as 190. The mesh in the x and y directions are uniform with $\Delta x = \Delta y$. The total number of grid cells is 3.68 million. The simulated 3D crescent wave case (up to 16 wave periods) required approximately 7 days to run in parallel on 32 processors on the supercomputing cluster at DTU.

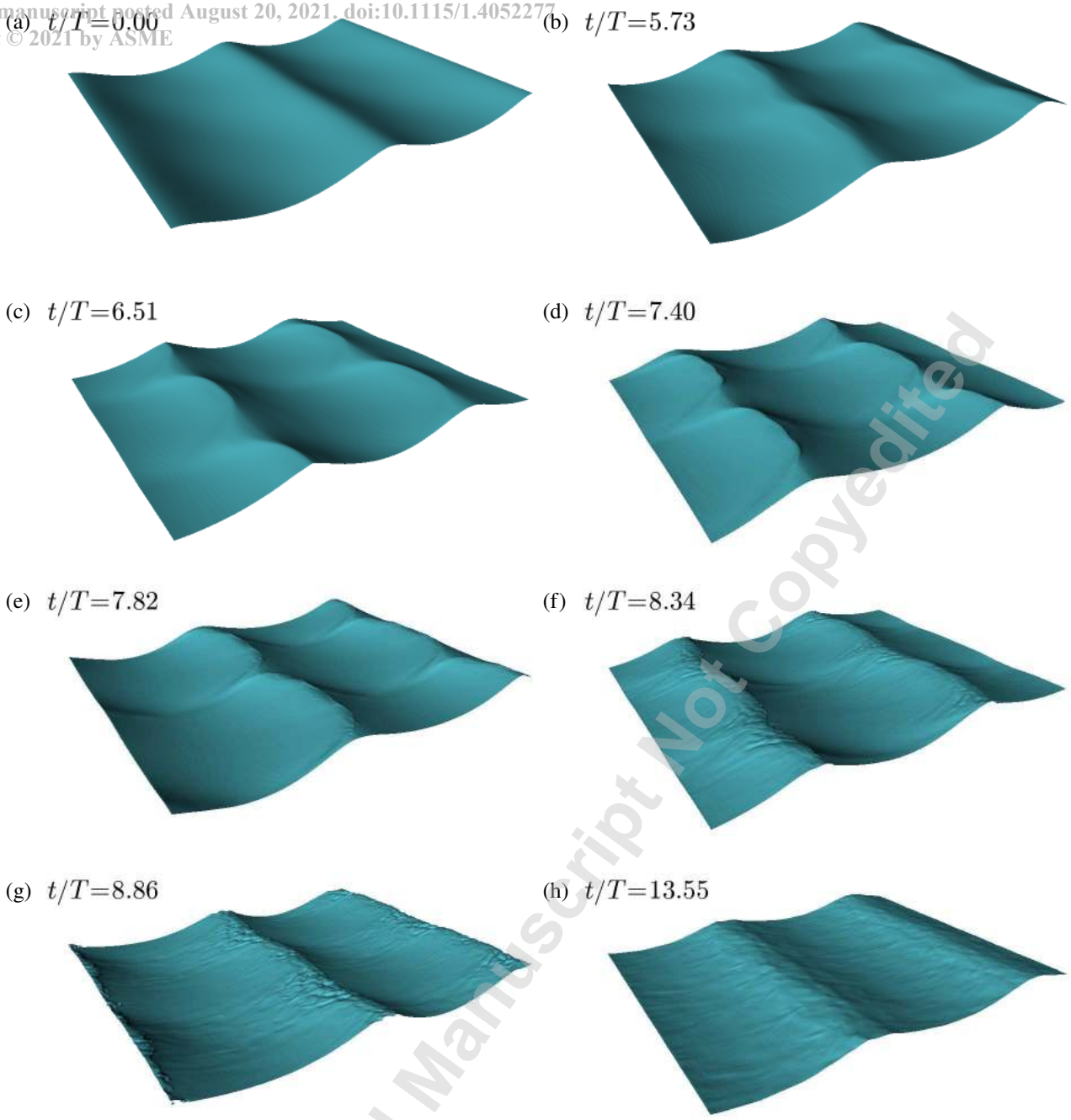

Fig. 6: Free surface evolution during the interaction between a plane wave train and 3D perturbations.

4.2 Results and Analysis

The 3D free surface patterns of crescent waves during the nonlinear evolution process are shown in Fig. 6. The free surfaces with multiple widths of the computed free surface are obtained by reflecting the simulated domain over the y-axis. Figure 6(a) shows the initial perturbed free surface profile which is approximately in 2D. In Fig. 6(b), a 3D wave feature starts to develop. From Fig. 6(c), clear crescent shapes start to emerge. The waves then become steeper in Fig. 6(d) with sharp triangular 'Delta' regions appearing on the front face. A clearer view of the 'Delta' regions in the front of the crescent forward fronts is provided in Fig. 7. Accompanied with the rising of the 'Delta' region and the crescent steepness, the crescent crests eventually break in the form of spilling breaker on the shoulders, as shown in Fig. 6(e) when the breaking just starts. The simulated L2 crescent wave as shown in Fig. 7 displays all the notable features that have been observed in the experiment in the basin of [17], i.e. the semicircular crests, steep shoulders, flat troughs and rising Delta regions on the front face.

In previous numerical studies based on potential flow theory (e.g. [12,13]), the simulations broke down at this initial breaking point ($t/T \approx 8$). The present CFD simulation is able to simulate the process during and beyond wave breaking. It is further seen in Fig. 6(f) that after the initial breaking, the free surface becomes turbulent, and the crescent shapes diminish.

Journal of Offshore Mechanics and Arctic Engineering. Received May 17, 2021;
Accepted manuscript posted August 20, 2021. doi:10.1115/1.4052277

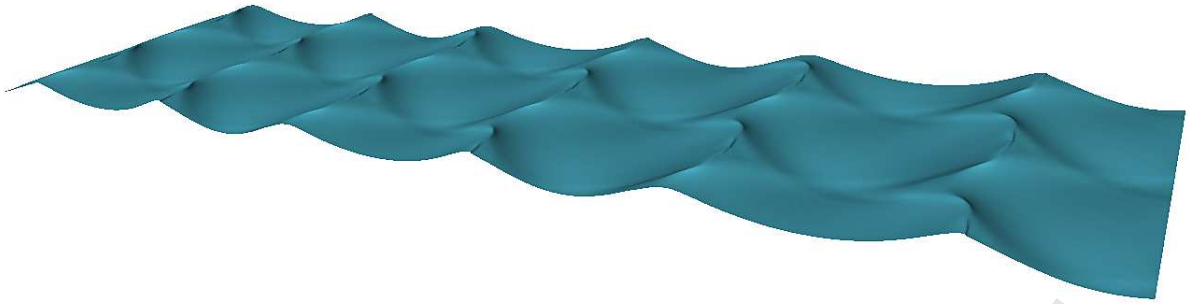

Fig. 7: Propagation of crescent waves at $t/T = 7.40$.

The wave steepness decreases due to energy dissipation in the breaking process and the 3D crescent pattern tends to go back to a nearly 2D form as shown in Fig. 6(g,h). It is seen in Fig. 6(h) that the waves finally decay to a status with a even flatter crest and trough compared to the initial status in Fig. 6(a). This overall process simulated with the present CFD model agrees with the observation of Su et al. in [29]. Their experiment showed that the crescent-shaped breaker quickly disappeared and the wave train returned to a more or less 2D form and with continuous modulations.

It is noted that with the occurrence of the crescent-shaped breaker, the wave surface becomes rough instead of the initial smooth surface. The present simulation incorporates the Reynolds stress turbulence model, therefore the 3D wave breaking process can be simulated. Moreover, the predicted rough surfaces for the crescent-shaped breaker, especially near the wave crest, look more like the observation in the wave tank (e.g. Figure 17 in [29]) than similar (preliminary) simulations with two-equation models which tend to smooth the wave surface.

For further quantitative analysis, the longitudinal profile of the L2 crescent waves along their centreline i.e. $y = L_y/2$ is presented in Fig. 8 at a representative time instant $t/T = 7.0$. The time instant is chosen because around the time of $t/T \sim 7$ an approximate quasi-steady state of crescent shape occurs and waves have not yet broken. A typical L2 feature is seen with the wave pattern repeated every other carrier wave length. The characteristic crescent wave geometric parameters computed from the present CFD model are compared with the measurement of Su [17] in Table 2. λ_2/λ_1 is the wavelength ratio between the alternating troughs. h_{11}/h_{12}, h_{21}/h_{22} and h_{11}/h_{21} are the characteristic wave height ratios. It is seen that the wavelength and wave height ratios match reasonably well with the experimental data. Similar computed results can be seen in e.g. [12, 13] with potential flow models.

The harmonic amplitudes of the carrier wave and the perturbation are shown in Fig. 9. The initial growth rate of the perturbations is verified against the theoretical prediction of McLean [2]. The theoretical line of the perturbation

	Experiment of Su [17]	Present CFD simulation ($t/T = 7.0$)
λ_2/λ_1	1.28	1.08
h_{11}/h_{12}	1.10	1.13
h_{21}/h_{22}	0.88	0.86
h_{11}/h_{21}	1.66	1.34

Table 2: The characteristic crescent wave geometric parameters computed from the present CFD model and the measurement of Su [17].

amplitude in Fig. 9 is expressed as:

$$\frac{a}{a_0} = \epsilon e^{0.0316\sqrt{gk_0}t} \tag{26}$$

It is seen that the initial exponential growth rate of the perturbation from the present CFD simulation matches very well with the theoretical prediction of McLean [2]. The perturbations continuously grow to a level that the wave starts to break ($t/T \approx 8$). During the wave breaking process, the harmonic amplitudes of both the carrier wave and perturbations are decreasing due to the turbulent energy dissipation ($t/T \approx$ 8-12.5). Finally, the amplitude of the carrier wave reduces about 20% and the perturbation amplitude decreases to an insignificant level.

Figure 10 presents turbulence levels just prior to, during and after wave breaking. Figure 10(a) shows a time instant before wave breaking while the crescent shape has already emerged. At this stage, the wave crests gradually become steeper but without turbulence generation beneath the wave surface. Figure 10(b) shows the turbulent kinetic energy during the initial wave breaking. Turbulence production is seen beneath the broken waves near the free surface. During the wave breaking process (around 4.5 wave periods), the turbulence level increases and turbulent kinetic energy is diffused downward to a greater depth beneath the free surface, as shown in Fig. 10(c) at the end of the wave breaking process. After breaking, the turbulent kinetic energy continuously dissipates and the wave steepness reduces to a

Journal of Offshore Mechanics and Arctic Engineering. Received May 17, 2021;
Accepted manuscript posted August 20, 2021. doi:10.1115/1.4052277

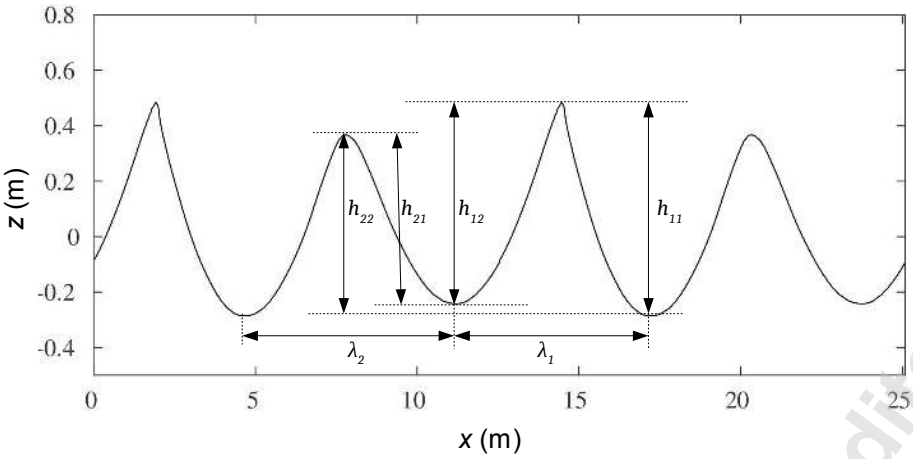

Fig. 8: Longitudinal profiles of the L2 crescent wave along the crescent centreline at $t/T = 4.3$.

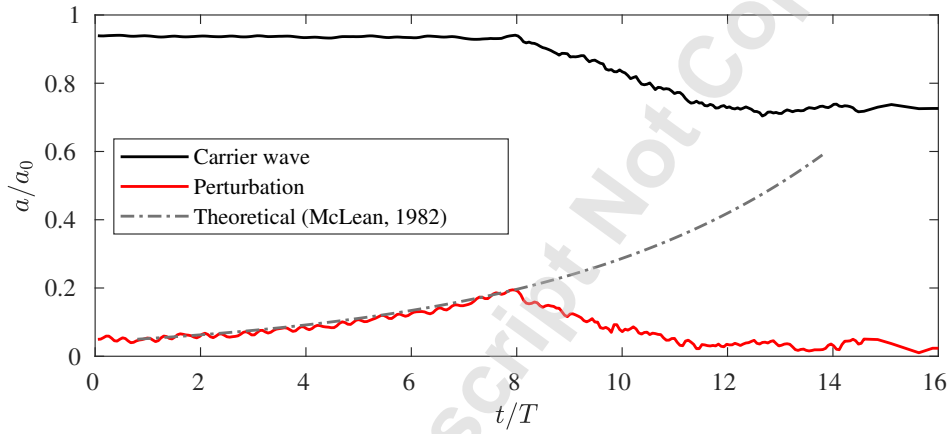

Fig. 9: Temporal evolution of the carrier wave and perturbation of the L2 crescent wave simulation.

non-breaking level, as shown in Fig. 10(d). It can also be observed that during the post-breaking stage, the turbulent kinetic energy continuously decays and diffuses downward. Near the free surface, the turbulence level has already reached an insignificant level. At this stage, the wave pattern returns back to a nearly 2D status, as presented earlier in Fig. 6(h). The wave steepness ($k_0a \approx 0.26$) of the resulting wave train post breaking is below the threshold where Class II instability dominates ($ka \approx 0.3$) [2]. The resulting wave train would still be unstable to Class I perturbations, however, as studied in Section 3.

5 Conclusions

The present study has focused on the numerical study of wave instability phenomena in terms of the 2D Benjamin-Feir instability (Class I type) and the 3D crescent waves (Class II type). The simulated cases in the present study have involved the wave breaking process. The Wilcox (2006) Reynolds stress-ω model has been applied for turbulence modelling due to its neutrally stable performance in the potential flow region beneath surface waves. The generation and development of wave instabilities from the initial evolution to the post-breaking status due to interaction between a plane wave train and perturbations have been investigated.

The present CFD model has been validated against a previous experiment of 2D Benjamin-Feir (Class I) instability involving wave breaking. The CFD results are in good agreement with the experimental data. The initial exponential growth rates of both sidebands are also verified against the analytical prediction. For Benjamin-Feir instability, our long-time simulation demonstrates the phenomenon of permanent frequency downshift after the occurrence of wave breaking.

For the 3D Class II crescent wave simulation, the initial growth rate of the perturbation is also consistent with the theoretical prediction. The present simulation has shown that the wave breaking process for the simulated crescent waves is brief (lasting for about 4.5 wave periods). The amplitude of the carrier wave decays about 20% during wave breaking.

Journal of Offshore Mechanics and Arctic Engineering. Received May 17, 2021;
Accepted manuscript posted August 20, 2021. doi:10.1115/1.4052277

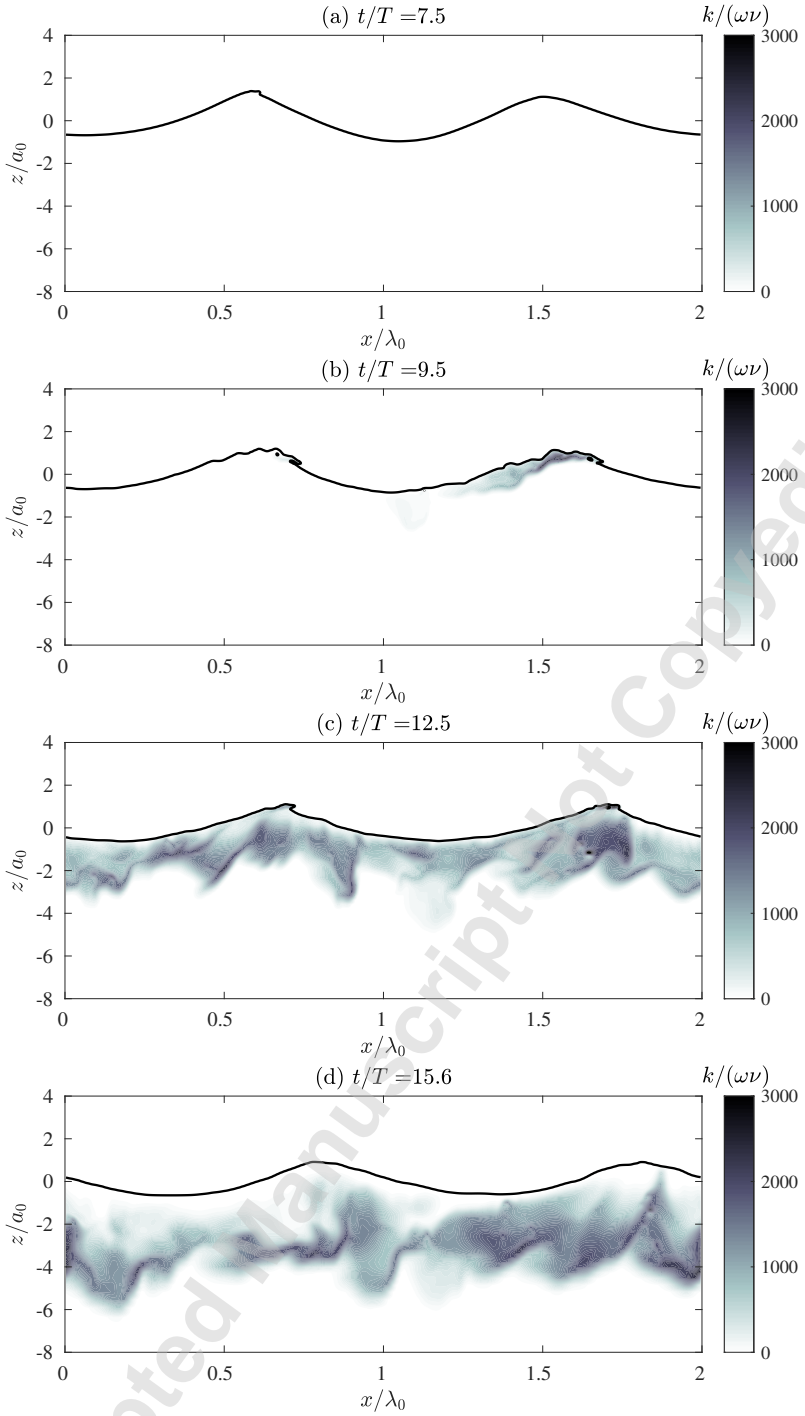

Fig. 10: Free surface (solid line) and turbulence levels beneath the surface waves during the nonlinear evolution of the L2 crescent waves ($y = L_y/2$).

After the crescent-shaped breaker disappears, the wave train returns to a nearly 2D form although with continuous three-dimensional modulations.

This is the first time a CFD model with proper turbulence modelling has been applied for simulating the Class I and Class II wave instability problems leading to breaking. In contrast to previous studies founded on potential flow theory which can only predict the wave evolution up to the breaking point or using artificial means of inducing dissipation due to breaking, the present study has been able to properly simulate the occurrence of wave breaking due to wave instabilities and investigate the wave evolution during and after breaking. By using a RANS-based Reynolds stress turbulence model, the computational cost for 3D two-phase breaking wave simulations becomes affordable, and the present approach is able to account for turbulence much more efficiently than the direct numerical simulation (DNS) and large eddy simulation (LES). The present study has shown that accompanied by

wave breaking, significant levels of turbulence are produced beneath the broken free surface. It is then diffused downward during the post-breaking wave evolution, before gradually decaying to insignificant levels.

Supplementary material

Animations for both the Class I (Benjamin-Feir) and II (crescent wave) simulations presented above can be found at: DOI:10.11583/DTU.14909949..

Acknowledgements

The first author acknowledges financial support from the European Union's Horizon 2020 research and innovation program, Marie Sklodowska- Curie Grant No. 713683 (COFUNDfellowsDTU, H. C. Ørsted Postdoc project SUBSEA: SimUlating Breaking waves and SEdiment trAnsport with stabilized turbulence models). The second author acknowledges financial support from the Independent Research Fund Denmark (project SWASH: Simulating WAve Surfzone Hydrodynamics and sea bed morphology, Grant No. 8022-00137B).

References

[1] Benjamin, T. B., and Feir, J., 1967. "The disintegration of wave trains on deep water". *J. Fluid. Mech.,* **27**(3), pp. 417–430.

[2] McLean, J. W., 1982. "Instabilities of finite-amplitude water waves". *J. Fluid. Mech.,* **114**, pp. 315–330.

[3] Tulin, M. P., and Waseda, T., 1999. "Laboratory observations of wave group evolution, including breaking effects". *J. Fluid. Mech.,* **378**, pp. 197–232.

[4] Hwung, H.-H., Chiang, W.-S., Yang, R.-Y., and Shugan, I. V., 2011. "Threshold model on the evolution of stokes wave side-band instability". *Eur. J. Mech. B Fluids,* **30**(2), pp. 147–155.

[5] Madsen, P. A., Bingham, H., and Liu, H., 2002. "A new boussinesq method for fully nonlinear waves from shallow to deep water". *J. Fluid. Mech.,* **462**, pp. 1–30.

[6] Iafrati, A., Babanin, A., and Onorato, M., 2013. "Modulational instability, wave breaking, and formation of large-scale dipoles in the atmosphere". *Phys. Rev. Lett.,* **110**(18), p. 184504.

[7] Iafrati, A., Babanin, A., and Onorato, M., 2014. "Modeling of ocean–atmosphere interaction phenomena during the breaking of modulated wave trains". *J. Comput. Phys.,* **271**, pp. 151–171.

[8] Alberello, A., and Iafrati, A., 2019. "The velocity field underneath a breaking rogue wave: Laboratory experiments versus numerical simulations". *Fluids,* **4**(2), p. 68.

[9] De Vita, F., Verzicco, R., and Iafrati, A., 2018. "Breaking of modulated wave groups: kinematics and energy dissipation processes". *J. Fluid. Mech.,* **855**, pp. 267–298.

[10] Tulin, M. P., 1996. "Breaking of ocean waves and downshifting". In *Waves and Nonlinear Processes in Hydrodynamics*. Springer, pp. 177–190.

[11] Deike, L., Melville, W. K., and Popinet, S., 2016. "Air entrainment and bubble statistics in breaking waves". *J. Fluid. Mech.,* **801**, pp. 91–129.

[12] Xue, M., Xü, H., Liu, Y., and Yue, D. K., 2001. "Computations of fully nonlinear three-dimensional wave-wave and wave-body interactions. part 1. dynamics of steep three-dimensional waves". *J. Fluid. Mech.,* **438**, pp. 11–39.

[13] Fuhrman, D. R., Madsen, P. A., and Bingham, H. B., 2004. "A numerical study of crescent waves". *J. Fluid. Mech.,* **513**, pp. 309–341.

[14] Fructus, D., Kharif, C., Francius, M., Kristiansen, Ø., Clamond, D., and Grue, J., 2005. "Dynamics of crescent water wave patterns". *J. Fluid. Mech.,* **537**, pp. 155–186.

[15] Xu, L., and Guyenne, P., 2009. "Numerical simulation of three-dimensional nonlinear water waves". *J. Comput. Phys,* **228**(22), pp. 8446–8466.

[16] Klahn, M., Madsen, P. A., and Fuhrman, D. R., 2020. "Simulation of three-dimensional nonlinear water waves using a pseudospectral volumetric method with an artificial boundary condition". *Int. J. Numer. Methods Fluids*, pp. 1843–1870.

[17] Su, M.-Y., 1982. "Three-dimensional deep-water waves. part 1. experimental measurement of skew and symmetric wave patterns". *J. Fluid. Mech.,* **124**, pp. 73–108.

[18] Jacobsen, N. G., Fuhrman, D. R., and Fredsøe, J., 2012. "A wave generation toolbox for the open-source cfd library: Openfoam®". *Int. J. Numer. Methods Fluids,* **70**(9), pp. 1073–1088.

[19] Wilcox, D., 2006. *Turbulence Modeling for CFD. 3rd edition*. DCW industries La Canada, CA.

[20] Li, Y., Larsen, B. E., and Fuhrman, D. R., 2021. "Reynolds stress turbulence modelling of surf zone breaking waves". *Submitted*.

[21] Brown, S., Greaves, D., Magar, V., and Conley, D., 2016. "Evaluation of turbulence closure models under spilling and plunging breakers in the surf zone". *Coast. Eng.,* **114**, pp. 177–193.

[22] Derakhti, M., Kirby, J. T., Shi, F., and Ma, G., 2016. "Wave breaking in the surf zone and deep-water in a non-hydrostatic RANS model. Part 2: Turbulence and mean circulation". *Ocean Modelling,* **107**, pp. 139–150.

[23] Devolder, B., Troch, P., and Rauwoens, P., 2018. "Performance of a buoyancy-modified k-ω and k-ω SST turbulence model for simulating wave breaking under regular waves using OpenFOAM". *Coast. Eng.,* **138**, pp. 49–65.

[24] Hsu, T. J., Sakakiyama, T., and Liu, P. L.-F., 2002. "A numerical model for wave motions and turbulence flows in front of a composite breakwater". *Coast. Eng.,* **46**(1), pp. 25–50.

[25] Larsen, B. E., and Fuhrman, D. R., 2018. "On the over-production of turbulence beneath surface waves in Reynolds-averaged Navier–Stokes models". *J. Fluid. Mech.,* **853**, pp. 419–460.

[26] Fuhrman, D. R., and Li, Y., 2020. "Instability of the realizable k-ε turbulence model beneath surface waves". *Phys. Fluids,* **32**(11). Article No. 115108.

[27] Shih, T.-H., Liou, W. W., Shabbir, A., Yang, Z., and Zhu, J., 1995. "A new k-ε eddy viscosity model for high Reynolds number turbulent flows". *Comput. Fluids,* **24**(3), pp. 227–238.

[28] Li, Y., Fredberg, M. B., Larsen, B. E., and Fuhrman, D. R., 2020. "Simulating breaking waves with the Reynolds stress turbulence model". *Coastal Engineering Proceedings*(36v), pp. 17–17.

[29] Su, M.-Y., Bergin, M., Marler, P., and Myrick, R., 1982. "Experiments on nonlinear instabilities and evolution of steep gravity-wave trains". *J. Fluid. Mech.,* **124**, pp. 45–72.

[30] Fenton, J., 1988. "The numerical solution of steady water wave problems". *Comput. Geosci.,* **14**(3), pp. 357–368.

[31] Larsen, B. E., Fuhrman, D. R., and Roenby, J., 2019. "Performance of interfoam on the simulation of progressive waves". *Coast. Eng. J.,* **61**(3), pp. 380–400.

[32] Melville, W., 1982. "The instability and breaking of deep-water waves". *J. Fluid. Mech.,* **115**, pp. 165–185.